# Soft Pneumatic Actuator Model Based on a Pressure-Dependent Spatial Nonlinear Rod Theory

Simon R. Eugster, Jonas Harsch, Max Bartholdt, Marco Herrmann, Mats Wiese, *Graduate Student Member, IEEE*, and Giuseppe Capobianco

***Abstract*—To describe the mechanical behavior of a soft pneumatic actuator, we present a nonlinear rod theory, which recognizes the chamber pressurization as contribution to the resultant contact forces and couples. Accordingly, the pressure actuation can be considered as part of the rod's constitutive laws, which relate the contact interactions with the rod's kinematics and the chamber pressures. The theory allows for nonlinear constitutive laws, which are capable of describing strengthening or softening behavior of largely deformable materials. The theory was applied to a three-chamber actuator to predict its centerline as well as the cross-section orientations in static equilibrium. The resulting governing equations were spatially discretized using beam finite elements. We evaluated four different actuator models that are contained in the presented theory regarding describability and predictability of the end effector position. Existing rod models with linear elastic material laws can describe the tip-displacement with an averaged deviation of 9.1 mm in the training set and 11.4 mm in the test set. With a deviation of 2.8 mm and 4.9 mm in the training and test set, respectively, the most enhanced model, for which the pressure chamber radii increase with increasing pressure, is more than 2 times more accurate.**

***Index Terms*—Modeling, control and learning for soft robots, soft sensors and actuators, flexible robotics.**

## I. Introduction

SOFT pneumatic actuators belong to a class of robotic systems whose actuation principle is based on the inflation of pressure chambers that are embedded within a soft material. With soft robotics gaining in popularity, many technical designs of soft pneumatic actuators have been developed [1]–[5]. Often, these type of actuators are employed in nature-inspired continuum robots for manipulation, see [6]. For the simulation of soft pneumatic actuators lumped-mass models [7], [8] as well as finite element models [9], [10] have been used. These approaches typically lead to models with a high number of degrees of freedom, which can be cumbersome for the control design. Due to the strong kinematic restriction, the constant-curvature approach leads to models with fewer degrees of freedom and has been used for the simulation and control of soft continuum robots [2], [11], [12]. However, these models require an extensive identification procedure and often perform well only for a subset of the workspace of the robot. Using rod theories [13], [14] to model soft pneumatic actuators, one can provide models with the predictive accuracy of the finite element method while keeping the number of degrees of freedom relatively low. Predominantly, spatial Cosserat rods with a linear elastic material law are used, where either the rods are spatially discretized using a finite element approach [4], [15] or the shooting method is invoked to solve the boundary value problem in the spatial dimension [16], [17].

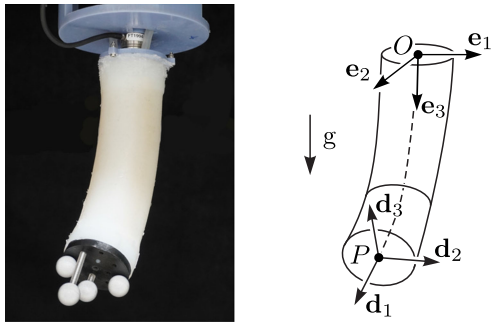


Fig. 1. (left) Picture of a soft pneumatic actuator with three pressure chambers. (right) Deformed configuration of a spatial rod.

In this letter, we derive a spatial rod theory with a nonlinear pressure-dependent constitutive law to model the 3-pressure-chamber actuator depicted in Fig. 1. In contrast to the derivation given in [16], where the laws of balance of linear and angular momenta for Cosserat rods were applied, we present here an alternative derivation starting from the principle of virtual work of the three-dimensional continuum. Moreover, we propose new model refinements that account for manufacturing imperfections as well as for the dilatation of the pressure chambers. To apply the model for control purposes, the unknown model parameters are experimentally identified, validated and compared with existing models.

Manuscript received August 31, 2021; accepted January 10, 2022. Date of publication January 25, 2022; date of current version January 28, 2022. This letter was recommended for publication by Associate Editor Carmel Majidi and Editor Cecilia Laschi upon evaluation of the reviewers' comments. This work was supported by the Deutsche Forschungsgemeinschaft (DFG), German Research Foundation, through the priority program 2100 Soft Material Robotic Systems under Grants 405032572 and 405032969. *(Simon R. Eugster and Jonas Harsch contributed equally to this work.) (Corresponding author: Simon R. Eugster.)*

Simon R. Eugster, Jonas Harsch, Marco Herrmann, and Giuseppe Capobianco are with the Institute for Nonlinear Mechanics, University of Stuttgart, 70569 Stuttgart, Germany (e-mail: eugster@inm.uni-stuttgart.de; harsch@inm.uni-stuttgart.de; st155898@stud.uni-stuttgart.de; giuseppe.capobianco@fau.de).

Max Bartholdt is with the Institute of Mechatronic Systems, Leibniz University Hannover, 30823 Hannover, Germany (e-mail: max.bartholdt@imes.uni-hannover.de).

Mats Wiese is with the Institute of Assembly Technology, Leibniz University Hannover, 30823 Hannover, Germany (e-mail: wiese@match.uni-hannover.de).

Digital Object Identifier 10.1109/LRA.2022.3144788

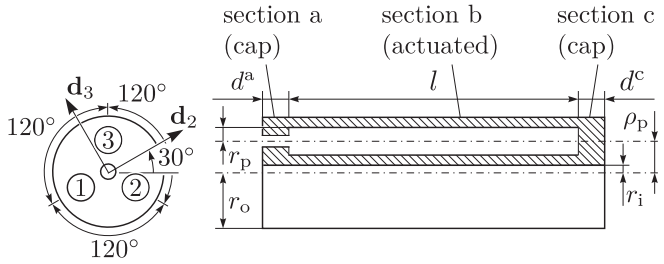


Fig. 2. Schematic design of the pneumatic actuator.

TABLE I
PARAMETERS OF THE SOFT PNEUMATIC ACTUATOR

| parameter | $l$ | $d^{\mathrm{a}}$ | $d^{\mathrm{c}}$ | $r_{\mathrm{o}}$ |
|---|---|---|---|---|
| value | 110 mm | 14 mm | 10 mm | 21.1 mm |
| parameter | $\rho_{\mathrm{p}}$ | $r_{\mathrm{p}}$ | $r_{\mathrm{i}}$ | |
| value | 12 mm | 5.15 mm | 2.9 mm | |

In Section II, we introduce the actuator, which is of cylindrical form with three cylindrical pressure chambers that are equidistantly distributed around the circumference and along the actuator length. The actuator can elongate and bend in three spatial directions depending on the applied pressure in the pressure chambers. The observed deformations suggest that a nonlinear constitutive behavior is needed to describe the actuator's deformation. Considering a rod as a constrained three-dimensional continuum, in Section III, a spatial theory for rods with pressurized chambers is derived. In Section IV, we specify the nonlinear strain energy functions used for the actuator models and introduce the above mentioned model refinements. The applicability of these strain energy functions is validated experimentally by experiments described in Section V. The model and the numerical solution procedure are discussed in Section VI. Therein, also the material parameters are identified and the predictive behavior of the model is validated and compared with existing models. The paper closes with a discussion and conclusion in Sections VII and VIII.

## II. SOFT PNEUMATIC ACTUATOR

The actuator was molded in multiple stages with 3D-printed casting molds. Three air chambers with a length of $110\,\mathrm{mm}$ were separately manufactured and reinforced with kevlar fiber to prevent large radial extension. The full actuator was molded in an upright position while the chambers were mechanically fixed in the casting and were standing on a cap of thickness $d^{\mathrm{c}} = 10\,\mathrm{mm}$. As depicted in Fig. 2, the chambers were arranged around the actuator's vertical axis with an angle of $120\,^\circ$ between the chambers. The cap encloses the ends of all air chambers. The actuator was completed by another cap of thickness $d^{\mathrm{a}} = 14\,\mathrm{mm}$ preserving one inlet per chamber for pneumatic tubes. Ecoflex™ 00-50 was used for all chambers and the intermediate section, which has a length of $l = 110\,\mathrm{mm}$. Both caps consist of comparatively stiff Dragon Skin™ 30. To support the reader's understanding, all geometric parameters are introduced in Fig. 2 and their values are listed in Table I.

For each chamber a solenoid valve continuously controls the in- and outgoing mass flow. The chamber is thereby either connected to the source pressure of 2 bar, the environment or isolated. Internal pressure is measured behind the solenoid valves, so that a suitable controller may be implemented. An open source EtherCAT solution is utilized as communication protocol for the test bench; see [18] for more information about the setup.

## III. ROD THEORY WITH PRESSURIZED CHAMBERS

The presented theory is formulated within the variational framework of the virtual work principle. Among other reasons, the variational formulation allows for a very elegant treatment of constrained media, as it is the case for the presented rod theory. When not otherwise indicated, Roman indices range between 1 and 3, Greek indices between 2 and 3.

Let $\mathbf{r} = \mathbf{r}(s) \in \mathbb{E}^3$ be a parametrization of a curve in the three-dimensional Euclidean vector space $\mathbb{E}^3$, which comes with the right-handed orthonormal basis $(\mathbf{e}_1, \mathbf{e}_2, \mathbf{e}_3)$. A classical nonlinear rod can be considered as a three-dimensional body whose placement function $\mathbf{x} : \mathbb{R}^3 \to \mathbb{E}^3$ is of the restricted form

$$\mathbf{x}(s, \theta^2, \theta^3) = \mathbf{r}(s) + \theta^2 \mathbf{d}_2(s) + \theta^3 \mathbf{d}_3(s)\,, \tag{1}$$

where the orthonormal directors $\mathbf{d}_i$ are related to the basis vectors $\mathbf{e}_i$ by a rotation $\mathbf{R} = \mathbf{R}(s) \in Orth^+$ in accordance with $\mathbf{d}_i(s) = \mathbf{R}(s)\mathbf{e}_i$. Consequently, the two directors $\mathbf{d}_\alpha$ span the rod's cross-sections, which remain rigid and plane throughout the deformation, see Fig. 1. The spatial curve $\mathbf{r}$ is called the centerline of the rod. The parameter $s$, which is also denoted by $\theta^1$, is chosen to be the arc length of the rod's centerline $\mathbf{r}_0$ in an undeformed reference configuration. The placement function (1) induces the co- and contravariant base vectors

$$\mathbf{g}_i = \frac{\partial \mathbf{x}}{\partial \theta^i}\,,\ \mathbf{g}^i = g^{-1/2}(\mathbf{g}_j \times \mathbf{g}_k)\,, \tag{2}$$

where $g^{1/2} = \mathbf{g}_1 \cdot (\mathbf{g}_2 \times \mathbf{g}_3)$ and where the construction of the contravariant base vectors $\mathbf{g}^i$ is valid for indices $(i, j, k)$ arising from an even permutation of (1,2,3). The admissible variation of the deformed configuration is induced by the variation of the centerline $\delta\mathbf{r}$ together with the variation of the directors

$$\delta\mathbf{d}_i = \delta\mathbf{R}\mathbf{R}^{\mathrm{T}}\mathbf{d}_i = \delta\boldsymbol{\phi} \times \mathbf{d}_i\,,\ \text{where } \delta\boldsymbol{\phi} = \mathrm{ax}(\delta\mathbf{R}\mathbf{R}^{\mathrm{T}}) \tag{3}$$

is the virtual rotation given by the axial vector to the skew symmetric tensor $\delta\mathbf{R}\mathbf{R}^{\mathrm{T}}$.

Considering a rod theory in the sense of an induced theory, [13], [14], [19], the internal virtual work of a rod with undeformed length $L$ is obtained as

$$\delta W^{\mathrm{int}} = -\int_0^L \{\mathbf{n} \cdot (\delta\mathbf{r}' - \delta\boldsymbol{\phi} \times \mathbf{r}') + \mathbf{m} \cdot \delta\boldsymbol{\phi}'\}\mathrm{d}s$$

$$\mathbf{n}(s) = \int_{A(s)} \mathbf{t}^1 \mathrm{d}\theta^2\mathrm{d}\theta^3\,,\ \mathbf{m}(s) = \int_{A(s)} \boldsymbol{\rho} \times \mathbf{t}^1 \mathrm{d}\theta^2\mathrm{d}\theta^3\,. \tag{4}$$

In (4), $\mathbf{n}$ and $\mathbf{m}$ are the resultant contact forces and couples, respectively, $A = A(s)$ denotes the cross-section area function and $\boldsymbol{\rho} = \mathbf{x} - \mathbf{r} = \theta^1\mathbf{d}_1 + \theta^2\mathbf{d}_2$ the lever arm to the stress vector $\mathbf{t}^1$, which is obtained from the Cauchy stress tensor $\boldsymbol{\sigma} = \boldsymbol{\sigma}(\mathbf{x}) \in$

$\mathrm{L}(\mathbb{E}^3;\mathbb{E}^3)$[1] by

$$\mathbf{t}^1 = g^{1/2}(\boldsymbol{\sigma}\circ\mathbf{x})\mathbf{g}^1 = (\boldsymbol{\sigma}\circ\mathbf{x})\mathbf{d}_1\,. \tag{5}$$

This relation originates from the derivation of (4) in [19], where the stress vector is defined as a part of the Cauchy stress in accordance with $\boldsymbol{\sigma}(\mathbf{x}(\theta^k)) = \sum_{i=1}^{3}(g^{-1/2}\mathbf{t}^i\otimes\mathbf{g}_i)(\theta^k)$.

The cross-section area can be split into the area $A_\mathrm{m} = A_\mathrm{m}(s)$ covered by the solid material and the areas of the $n_\mathrm{ch}$ pressure chambers $A_{\mathrm{p}_k} = A_{\mathrm{p}_k}(s), k = 1,\ldots,n_\mathrm{ch}$. Indicating by $\mathrm{m}$ and $\mathrm{p}$ the material and pressurized part, due to (4), the contact forces $\mathbf{n}$ and contact couples $\mathbf{m}$ can be decomposed into

$$\begin{aligned}\mathbf{n}_\mathrm{m}+\mathbf{n}_\mathrm{p} &= \int_{A_\mathrm{m}}\mathbf{t}^1\mathrm{d}\theta^2\mathrm{d}\theta^3 + \sum_{k=1}^{n_\mathrm{ch}}\int_{A_{\mathrm{p}_k}}\mathbf{t}^1\mathrm{d}\theta^2\mathrm{d}\theta^3\,,\\ \mathbf{m}_\mathrm{m}+\mathbf{m}_\mathrm{p} &= \int_{A_\mathrm{m}}\boldsymbol{\rho}\times\mathbf{t}^1\mathrm{d}\theta^2\mathrm{d}\theta^3 + \sum_{k=1}^{n_\mathrm{ch}}\int_{A_{\mathrm{p}_k}}\boldsymbol{\rho}\times\mathbf{t}^1\mathrm{d}\theta^2\mathrm{d}\theta^3\,.\end{aligned} \tag{6}$$

For a constant pressure distribution $p_k$ within the $k$th pressure chamber, the Cauchy stress is known as $-p_k\mathbf{I}$, where $\mathbf{I}$ denotes the identity tensor on $\mathbb{E}^3$. Using (5) within (6), the pressurized part of the contact forces and couples can be computed as

$$\mathbf{n}_\mathrm{p} = -\sum_{k=1}^{n_\mathrm{ch}} p_k A_{\mathrm{p}_k}\mathbf{d}_1\,,\ \mathbf{m}_\mathrm{p} = -\sum_{k=1}^{n_\mathrm{ch}}\boldsymbol{\rho}_k\times(p_k A_{\mathrm{p}_k}\mathbf{d}_1)\,. \tag{7}$$

Here, $\boldsymbol{\rho}_k = \boldsymbol{\rho}_k(s)$ is the vector between the centerline and the line of centroids of the $k$th pressure chamber obtained by

$$\int_{A_{\mathrm{p}_k}}\boldsymbol{\rho}\,\mathrm{d}\theta^2\mathrm{d}\theta^3 = \boldsymbol{\rho}_k A_{\mathrm{p}_k}\,. \tag{8}$$

Let $s_1 = 0$ and $s_2 = L$, then the external virtual work can be written as

$$\begin{aligned}\delta W^\mathrm{ext} = &\int_0^L\{\delta\mathbf{r}\cdot\overline{\mathbf{n}}+\delta\boldsymbol{\phi}\cdot\overline{\mathbf{m}}\}\mathrm{d}s\\ &+\sum_{i=1}^{2}\{\delta\mathbf{r}(s_i)\cdot\overline{\mathbf{n}}_{s_i}+\delta\boldsymbol{\phi}(s_i)\cdot\overline{\mathbf{m}}_{s_i}\}\,,\end{aligned} \tag{9}$$

where $\overline{\mathbf{n}} = \overline{\mathbf{n}}(s)$ and $\overline{\mathbf{m}} = \overline{\mathbf{m}}(s)$ denote the distributed external forces and couples, respectively, and $\overline{\mathbf{n}}_0$, $\overline{\mathbf{n}}_L$, $\overline{\mathbf{m}}_0$ and $\overline{\mathbf{m}}_L$ are external forces and couples applied at the rod's boundaries.

Using the principle of virtual work, which demands the total virtual work $\delta W^\mathrm{tot} = \delta W^\mathrm{int} + \delta W^\mathrm{ext}$ to vanish for all virtual displacements admissible to (1), the equilibrium conditions for the rod follow by a straight forward integration by parts procedure, see [20]. These conditions are given by the boundary value problem with the set of ordinary differential equation

$$\begin{aligned}0 &= \mathbf{n}_\mathrm{m}' + \mathbf{n}_\mathrm{p}' + \overline{\mathbf{n}}\\ 0 &= \mathbf{m}_\mathrm{m}' + \mathbf{r}'\times\mathbf{n}_\mathrm{m} + \mathbf{m}_\mathrm{p}' + \mathbf{r}'\times\mathbf{n}_\mathrm{p} + \overline{\mathbf{m}}\end{aligned} \tag{10}$$

together with the boundary conditions

$$\begin{aligned}\mathbf{n}_\mathrm{m}(0) &= -\overline{\mathbf{n}}_0 - \mathbf{n}_\mathrm{p}(0)\,, &\mathbf{m}_\mathrm{m}(0) &= -\overline{\mathbf{m}}_0 - \mathbf{m}_\mathrm{p}(0)\,,\\ \mathbf{n}_\mathrm{m}(L) &= \overline{\mathbf{n}}_L - \mathbf{n}_\mathrm{p}(L)\,, &\mathbf{m}_\mathrm{m}(L) &= \overline{\mathbf{m}}_L - \mathbf{m}_\mathrm{p}(L)\,.\end{aligned} \tag{11}$$

[1] $\mathrm{L}(\mathbb{E}^3;\mathbb{E}^3)$ denotes the set of linear maps $f:\mathbb{E}^3\to\mathbb{E}^3$.

Since the pressure distribution within the chambers are assumed to be known, it is justified to argue that the pressurized chambers induce the external distributed forces $\overline{\mathbf{n}}_\mathrm{p} = \mathbf{n}_\mathrm{p}'$ and couples $\overline{\mathbf{m}}_\mathrm{p} = \mathbf{m}_\mathrm{p}' + \mathbf{r}'\times\mathbf{n}_\mathrm{p}$ as well as the external forces and couples at the boundaries $\overline{\mathbf{n}}_{\mathrm{p},0} = \mathbf{n}_\mathrm{p}(0)$, $\overline{\mathbf{n}}_{\mathrm{p},L} = -\mathbf{n}_\mathrm{p}(L)$, $\overline{\mathbf{m}}_{\mathrm{p},0} = \mathbf{m}_\mathrm{p}(0)$, $\overline{\mathbf{m}}_{\mathrm{p},L} = -\mathbf{m}_\mathrm{p}(L)$. Indeed, there is an alternative way to derive the equilibrium equations. The known pressure distribution in the pressure chambers cause surface force distributions on their top, bottom and lateral surfaces. Using the virtual work contribution of surface forces for a three-dimensional continuum together with the restricted rod kinematics (1) leads after some computations to the just mentioned force and couple contributions. However, these computations are easy to handle only for the special case, where the distance between the centerline and the line of centroids $\boldsymbol{\rho}_k$ as well as the areas $A_{\mathrm{p}_k}$ are constant functions. For this particular case, the equilibrium equations (10) correspond with the static version of the equations given in [16] below equation (18).

Considering the solid material to be hyperelastic, the most general objective strain energy function for this part of the rod is a function $W = W(\Gamma_i,\kappa_i;s)$, which depends on the strain measures

$$\Gamma_i = \mathbf{d}_i\cdot\mathbf{r}'\,,\quad \kappa_i = \sum_{j,k=1}^{3}\frac{1}{2}\varepsilon_{ijk}(\mathbf{d}_k\cdot\mathbf{d}_j') \tag{12}$$

and which may depend on the arc length parameter $s$, see [20]. With $\varepsilon_{ijk}$ the Levi-Civita permutation symbol is meant. For indices $(i,j,k)$ being an even permutation of (1,2,3), the Levi-Civita symbol evaluates to 1, for an odd permutation to $-1$ and zero else. According to [13, Section 6, p. 285], $\Gamma_1$ measures dilatation, $\Gamma_2$ and $\Gamma_3$ shear, $\kappa_1$ torsion, and $\kappa_2$ and $\kappa_3$ flexure. The centerline stretch is considered as the ratio between the deformed and the undeformed length of the centerline's tangents. Due to the parameterization by the reference arc length ($\|\mathbf{r}_0'\| = 1$), the stretch is used here as the function

$$\lambda(\Gamma_i(s)) = [\Gamma_1(s)^2+\Gamma_2(s)^2+\Gamma_3(s)^2]^{1/2} = \|\mathbf{r}'(s)\|\,. \tag{13}$$

For the sake of brevity, we will often omit the concatenation with $\Gamma_i$ when requiring the stretch as a function of $s$. As shown in [20], the contact forces and contact couples for the hyperelastic solid material are of the form

$$\mathbf{n}_\mathrm{m} = \sum_{i=1}^{3}\frac{\partial W}{\partial\Gamma_i}\mathbf{d}_i\,,\quad \mathbf{m}_\mathrm{m} = \sum_{i=1}^{3}\frac{\partial W}{\partial\kappa_i}\mathbf{d}_i\,. \tag{14}$$

## IV. Specific Strain Energy Functions

To model the manufactured pneumatic actuator presented in Section II, we propose strain energy functions of the form

$$W(\Gamma_i,\kappa_i;s) = W_1(\lambda(\Gamma_i);s) + W_2(\Gamma_i,\kappa_i;s)\,. \tag{15}$$

According to [21], a highly nonlinear material model is required to represent the stress-strain relations of the used materials during an uniaxial extension test. Hence, we assume in axial direction the strain energy

$$W_1 = \frac{2}{3}\frac{k_\mathrm{e}}{\alpha^2}(\lambda^\alpha + 2\lambda^{-\alpha/2} - 3)\,, \tag{16}$$

TABLE II
MATERIAL PARAMETER OF ACTUATOR

| | | | |
|---|---|---|---|
| $E_{\text{Ecoflex}}$ | $0.08\,\text{N}\,\text{mm}^{-2}$ | $E_{\text{DragonSkin}}$ | $0.6\,\text{N}\,\text{mm}^{-2}$ |
| $G_{\text{Ecoflex}}$ | $0.027\,\text{N}\,\text{mm}^{-2}$ | $G_{\text{DragonSkin}}$ | $0.2\,\text{N}\,\text{mm}^{-2}$ |
| $\rho_{0,\text{Ecoflex}}$ | $1070\,\text{kg}\,\text{m}^{-3}$ | $\rho_{0,\text{DragonSkin}}$ | $1080\,\text{kg}\,\text{m}^{-3}$ |

which follows from an Ogden material [22, (4.3.66)] when using the following assumptions. Only one parameter pair $\mu$ and $\alpha$ is used. The energy describes the case for an incompressible material under uniaxial extension with axisymmetric contraction [22, (2.2.47)]. Lastly, the parameter $\mu$ is expressed in terms of the extensional stiffness $k_\text{e}$ as $\mu = 2k_\text{e}/3\alpha$. By a Taylor expansion up to second order around the undeformed state $\lambda = 1$, it can readily be seen that $W_1 = 0.5k_\text{e}(\lambda - 1)^2 + o(\lambda^2)$. For the extensional stiffness, Saint-Venant's relations from linear elasticity, scaled by a factor $c_\text{e}$, is used, i.e.,

$$k_\text{e} = c_\text{e} E A_\text{m}\,, \tag{17}$$

where $E$ denotes the Young's modulus of the used material. Moreover, $A_\text{m}$ is the cross-section area covered by the material.

To represent a general anisotropic bending behavior with bending stiffnesses $k_{\text{b}_2}$, $k_{\text{b}_3}$ and $k_{\text{b}_{23}}$, the energy $W_2$ for bending, shear and torsion is assumed to be of the form

$$W_2 = \frac{1}{2}\left(k_\text{s}[\Gamma_2^2 + \Gamma_3^2] + k_\text{t}\kappa_1^2 + + k_{\text{b}_2}\kappa_2^2 + k_{\text{b}_3}\kappa_3^2 + 2k_{\text{b}_{23}}\kappa_2\kappa_3\right). \tag{18}$$

For the shear and torsional stiffnesses, again Saint-Venant's relations from linear elasticity are used, i.e.,

$$k_\text{s} = G A_\text{m}\,, \quad k_\text{t} = G J_\text{m}\,, \tag{19}$$

where $G$ denotes the shear modulus of the used material. Further, $J_\text{m} = I_{2,\text{m}} + I_{3,\text{m}}$ denotes the material part of the rod's polar moment of inertia with respect to its centerline defined by the second moments of area with respect to the $\mathbf{d}_2$- and $\mathbf{d}_3$-axis $I_{2,\text{m}}$ and $I_{3,\text{m}}$, respectively.

For the bending stiffnesses, we introduce a correction factor $c_\text{b}$, which scales the relation from linear elasticity. For $A \in \{2, 3, 23\}$, the stiffnesses are computed as

$$k_{\text{b}_A} = c_\text{b} E I_{A,\text{m}}\,. \tag{20}$$

Thus, the strain energy functions are formulated in such a way, that only the parameters $c_\text{e}$, $\alpha$ and $c_\text{b}$ have to be determined experimentally. The remaining parameters are either of geometric nature or are taken from material data sheets. The specific geometric quantities of the actuator, see Fig. 2, are listed in Table I. The relevant formulas for area and second moment of area for the respective parts are given in Table III. Here, the superscripts a, b and c denote the respective parts of the actuator. Further, the material properties extracted from the material sheets of the two silicones Ecoflex 00-50 and Dragon Skin 30 together with an assumed Poisson's ratio of $\nu = 0.5$ are listed in Table II.

The experimentally obtained data, which are presented in Section V, inspired the following two refinements of the model. First, imperfections of the manufacturing can cause an offset

TABLE III
AREAS AND SECOND MOMENTS OF AREAS

| | |
|---|---|
| $A_\text{o}$ | $\pi r_\text{o}^2$ |
| $A_\text{i}$ | $\pi r_\text{i}^2$ |
| $A_{\text{p}_k}$ | $\pi r_{\text{p}_k}^2$ |
| $A_\text{m}^\text{a} = A_\text{m}^\text{c}$ | $A_\text{o} - A_\text{i}$ |
| $A_\text{m}^\text{b}$ | $A_\text{o} - A_\text{i} - \sum_{k=1}^3 A_{\text{p}_k}$ |
| $I_{2,\text{o}} = I_{3,\text{o}}$ | $\frac{\pi}{4} r_\text{o}^4$ |
| $I_{2,\text{i}} = I_{3,\text{i}}$ | $\frac{\pi}{4} r_\text{i}^4$ |
| $I_{23,\text{o}} = I_{23,\text{i}}$ | $0$ |
| $I_{2,p_k}$ | $\frac{\pi}{4} r_{p_k}^4 + \rho_{k,3}^2 A_{\text{p}_k}$ |
| $I_{3,p_k}$ | $\frac{\pi}{4} r_{p_k}^4 + \rho_{k,2}^2 A_{\text{p}_k}$ |
| $I_{23,p_k} = I_{32,p_k}$ | $-\rho_{k,2}\rho_{k,3} A_{\text{p}_k}$ |
| $I_{A,\text{m}}^\text{a} = I_{A,\text{m}}^\text{c}$ | $I_{A,\text{o}} - I_{A,\text{i}}$ |
| $I_{A,\text{m}}^\text{b}$ | $I_{A,\text{o}} - I_{A,\text{o}} - \sum_{k=1}^3 I_{A,\text{p}_k}$ |

in the vector $\boldsymbol{\rho}_k = \rho_{k,2}\mathbf{d}_2 + \rho_{k,3}\mathbf{d}_3$ between the centerline and the line of centroids of the $k$th pressure chamber. To account for this effect, we introduce a constant vector $\boldsymbol{\rho}^\text{off}$ which leads in agreement with the ideal geometry of Fig. 2 to

$$\begin{aligned}\boldsymbol{\rho}_1 &= -\rho_\text{p}\mathbf{d}_2 + \boldsymbol{\rho}^\text{off}\,,\\ \boldsymbol{\rho}_\alpha &= \rho_\text{p}\left(\frac{1}{2}\mathbf{d}_2 - (-1)^\alpha\frac{\sqrt{3}}{2}\mathbf{d}_3\right) + \boldsymbol{\rho}^\text{off}\,.\end{aligned} \tag{21}$$

This offset results in a non-symmetric excitation also for equal pressure level in all three chambers. In accordance with (7), this imperfection affects the equilibrium equations linearly. Due to Steiner-Huygens theorem, the bending and torsional stiffnesses are modified only quadratically by this imperfection.

The second refinement is to account in a heuristic way for the cross-section deformation. In fact, we assume the pressure to cause a dilatation of the chambers resulting in a pressure-dependent radius

$$r_{\text{p}_k}(p) = r_\text{p}\left(1 + c_\text{p}\frac{p}{p_\text{ref}}\right)\,, \tag{22}$$

where $c_\text{p}$ is an experimentally determined constant and $p_\text{ref}$ denotes the reference pressure for which the radius is extended by the factor $1 + c_\text{p}$. The change in radius increases the contact forces and couples due to the pressure (7) but also affects the stiffnesses of the material part in section b, see (17), (19) and (20) with the now pressure-dependent geometric values computed as in Table III. Consequently, the strain energy function (15) must be considered as a function $W = W(\Gamma_i, \kappa_i; s, p_k)$, which depends also explicitly on the pressure values $p_k$.

## V. EXPERIMENTAL SETUP AND RESULTS

In the two experimental setups *horizontal mounting* and *vertical mounting* as depicted in Figs. 3 and 4, the actuator was mounted at the end of the first cap (section a) in horizontal and vertical configuration, respectively. The pressure chambers were adjusted in accordance with the drawings. Also the inertial frames and the rod's director triads for the corresponding reference configuration are depicted therein. At the end of the actuator, a plate with four spherical markers was attached to recognize the pose of the rod's last director frame. The overall

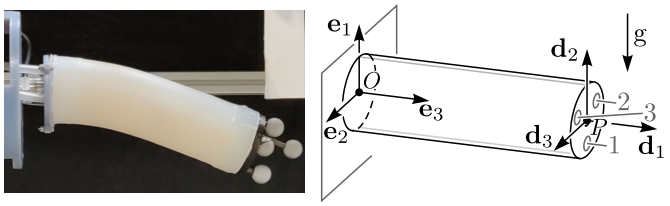


Fig. 3. Chamber arrangement and frame definitions for experimental setup *horizontal mounting*.

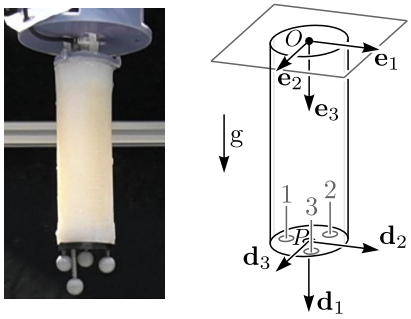


Fig. 4. Chamber arrangement and frame definitions for experimental setup *vertical mounting*.

marker system had a mass of $m_{\text{marker}} = 1.725 \cdot 10^{-2}$ kg. The vector between the actuator's end point $P$ and the center of mass of the marker system is $\boldsymbol{\rho}_{\text{marker}} = 9.3\mathbf{d}_1 + 2.9\mathbf{d}_2 - 1.1\mathbf{d}_3$. The components are given in [mm] and the director triad is evaluated at the end of the second cap. The used camera system (Prime 17 W, OptiTrack) resolves the position of the markers with an error below 1 mm and returns the coordinates $(\bar{x}, \bar{y}, \bar{z})$ of the actuator's end point $P$ with respect to the inertial frame $\mathbf{e}_i$, i.e.,

$$\mathbf{r}_{OP} = \bar{x}\mathbf{e}_1 + \bar{y}\mathbf{e}_2 + \bar{z}\mathbf{e}_3 \ . \tag{23}$$

In the experiments, the pressure levels of the individual chambers were changed. To avoid transient effects due to inertia and pressure build-up, the pressure levels were increased in 30 equal steps and decreased again in another 30 steps. Each pressure level was kept for 10 s.

*a) Horizontal mounting:* In a horizontal configuration, as depicted in Fig. 3, the pressure levels of chamber 1, $p_1 = p$, was changed while $p_2 = p_3 = 0$. The pressure level $p$ was increased from $0\,bar$ up to $0.6\,bar$. The pressure levels and coordinates of the actuator's end point $P$ are plotted in Fig. 5 (top). For the case of zero pressure, $p_i = 0$, the end point was at

$$\overline{x} = -34.5\,\text{mm}\,,\ \overline{y} = 2.8\,\text{mm}\,,\ \overline{z} = 130.8\,\text{mm}\,. \tag{24}$$

*b) Vertical mounting:* In a vertical configuration, as depicted in Fig. 4, the pressure level $p$ was increased from $0\,bar$ up to $0.6\,bar$.

i) Three measurements were carried out in which one chamber was pressurized $p_i = p$ and $p_j = p_k = 0$. The pressure levels and coordinates of the actuator's end point $P$ are plotted in Fig. 6.

ii) Three measurements were carried out in which two chambers were pressurized $p_i = 0$ and $p_j = p_k = p$. The pressure levels and and coordinates of the actuator's end point $P$ are plotted in Fig. 7.

iii) All three chambers were pressurized with the same pressure level $p_i = p$. The pressure levels and the coordinates of the actuator's end point $P$ are plotted in Fig. 5 (bottom).

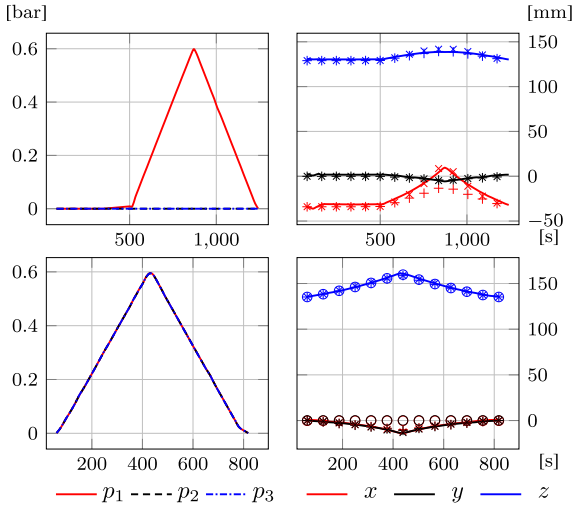


Fig. 5. (top left) Chamber pressures for experiment a) horizontal mounting, $p_1 = p$ and $p_2 = p_3 = 0$. (bottom left) Chamber pressures for experiment (iii), $p_1 = p_2 = p_3 = p$. (right) End effector position coordinates w.r.t. respective $\mathbf{e}_i$-system. The measured quantities are indicated by solid lines. The circles, pluses and crosses indicate the simulated results for actuator models M1, M2 and M3 respectively.

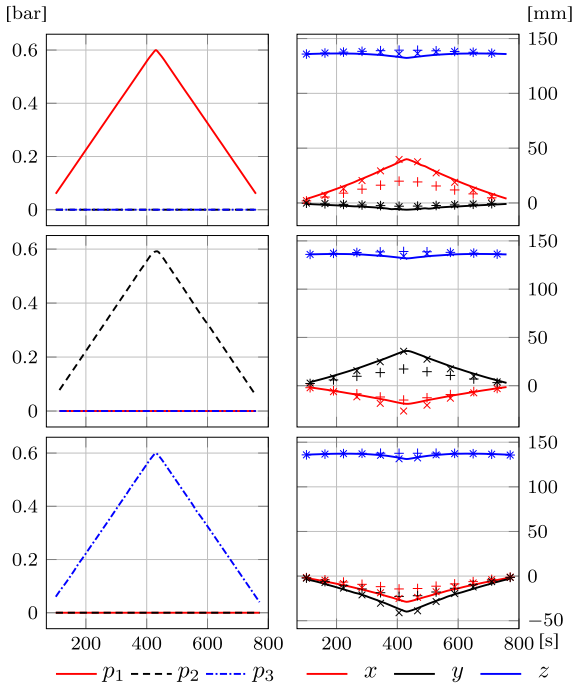


Fig. 6. (left) Chamber pressures for experiment $(i)$, $p_i = p$ and $p_j = p_k = 0$. (right) End effector position coordinates w.r.t. $\mathbf{e}_i$-system. The measured quantities are indicated by solid lines. The pluses and crosses indicate the simulated results for actuator models M2 and M3, respectively.

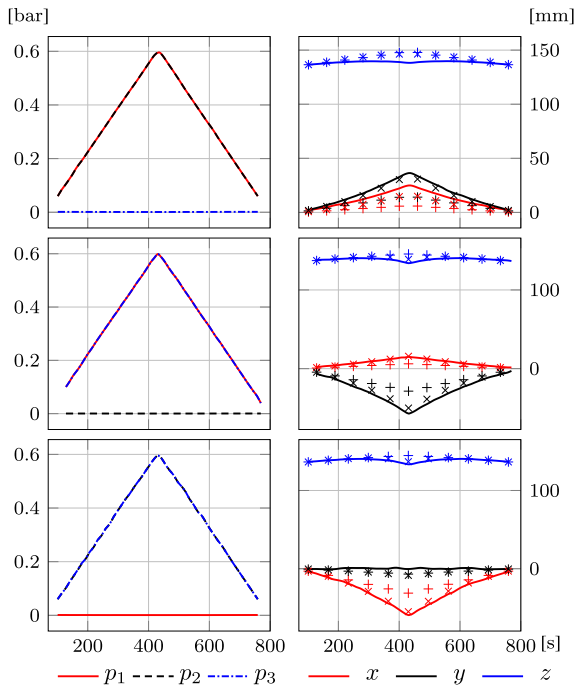


Fig. 7. (left) Chamber pressures for experiment (ii), $p_i = 0$ and $p_j = p_k = p$. (right) End effector position coordinates w.r.t. $\mathbf{e}_i$-system. The measured quantities are indicated by solid lines. The pluses and crosses indicate the simulated results for actuator models M2 and M3, respectively.

## VI. Modeling and Parameter Identification

To show the applicability of the proposed rod theory, the following model of the overall experimental setup is formulated. The caps of the actuator (section a and c) are modeled by two rods of reference lengths $d^{\mathrm{a}}$ and $d^{\mathrm{c}}$, respectively, with the material data of Dragon Skin™ 30. The correction factors $c_{\mathrm{e}}$, $c_{\mathrm{b}}$ as well as $\alpha$ are all set to 1. The central part (section b) is another rod of reference length $l$ made of Ecoflex™ 00-50 with to be determined parameters $c_{\mathrm{e}}$, $c_{\mathrm{b}}$ and $\alpha$. The material and geometric data are listed in Tables II and III. The unknowns of the model are thus the centerlines $\mathbf{r}^{\mathrm{a}}, \mathbf{r}^{\mathrm{b}}, \mathbf{r}^{\mathrm{c}}$ as well as the cross-section rotations that lead to the director frames $\mathbf{d}_i^{\mathrm{a}}, \mathbf{d}_i^{\mathrm{b}}, \mathbf{d}_i^{\mathrm{c}}$. The three rods are rigidly connected such that the two vector-valued constraint functions must be satisfied

$$\mathbf{g}_{\mathrm{ab}} = \begin{pmatrix} \mathbf{r}^{\mathrm{a}}(d^{\mathrm{a}}) - \mathbf{r}^{\mathrm{b}}(0) \\ \mathbf{d}_1^{\mathrm{a}}(d^{\mathrm{a}}) \cdot \mathbf{d}_2^{\mathrm{b}}(0) \\ \mathbf{d}_2^{\mathrm{a}}(d^{\mathrm{a}}) \cdot \mathbf{d}_3^{\mathrm{b}}(0) \\ \mathbf{d}_3^{\mathrm{a}}(d^{\mathrm{a}}) \cdot \mathbf{d}_1^{\mathrm{b}}(0) \end{pmatrix}, \quad \mathbf{g}_{\mathrm{bc}} = \begin{pmatrix} \mathbf{r}^{\mathrm{b}}(l) - \mathbf{r}^{\mathrm{c}}(0) \\ \mathbf{d}_1^{\mathrm{b}}(l) \cdot \mathbf{d}_2^{\mathrm{c}}(0) \\ \mathbf{d}_2^{\mathrm{b}}(l) \cdot \mathbf{d}_3^{\mathrm{c}}(0) \\ \mathbf{d}_3^{\mathrm{b}}(l) \cdot \mathbf{d}_1^{\mathrm{c}}(0) \end{pmatrix}. \quad (25)$$

Additionally, the first rod is clamped in the origin and satisfies the constraints

$$\mathbf{g}_{\mathrm{clamping}} = (\mathbf{r}^{\mathrm{a}}(0),\ \mathbf{d}_1^{\mathrm{a}}(0) \cdot \mathbf{e}_2,\ \mathbf{d}_2^{\mathrm{a}}(0) \cdot \mathbf{e}_3,\ \mathbf{d}_3^{\mathrm{a}}(0) \cdot \mathbf{e}_1)\,. \quad (26)$$

For all three rods, the effects due to gravity are taken into account by the line force distribution

$$\overline{\mathbf{n}} = \rho_0 A_{\mathrm{m},0} \mathbf{g}\,, \quad (27)$$

TABLE IV
Identified Parameters

| | | | | | | |
|---|---|---|---|---|---|---|
| *M0* | $c_{\mathrm{b}}$ 1.31 | $c_{\mathrm{e}}$ 0.92 | | | | |
| *M1* | $c_{\mathrm{b}}$ 1.31 | $c_{\mathrm{e}}$ 2.95 | $\alpha$ 0.61 | | | |
| *M2* | $c_{\mathrm{b}}$ 1.31 | $c_{\mathrm{e}}$ 3.10 | $\alpha$ 0.62 | $\theta^{\mathrm{off},2}$ 1.46 mm | $\theta^{\mathrm{off},3}$ 1.64 mm | |
| *M3* | $c_{\mathrm{b}}$ 1.31 | $c_{\mathrm{e}}$ 2.82 | $\alpha$ 8.89 | $\theta^{\mathrm{off},2}$ 0.89 mm | $\theta^{\mathrm{off},3}$ 0.98 mm | $c_{\mathrm{p}}$ 0.48 |

Since the inertial system is changed between the horizontal and vertical mounting, the gravity vector is either $\mathbf{g} = \mathrm{g}\mathbf{e}_3$ or $\mathbf{g} = -\mathrm{g}\mathbf{e}_1$ with gravity constant $\mathrm{g} = 9.81\,\mathrm{m/s^2}$ and the respective referential volume density $\rho_0$ specified in Table II. Note, $A_{\mathrm{m},0}$ is the referential area, i.e., $A_{\mathrm{m}}$ for $p_k = 0$. The gravitational effect of the marker system is taken into account by a force and couple at the third rod's end $s = d^{\mathrm{c}}$, these are

$$\overline{\mathbf{n}}_{d^{\mathrm{c}}} = m_{\mathrm{marker}} \mathbf{g}\ \ \overline{\mathbf{m}}_{d^{\mathrm{c}}} = \boldsymbol{\rho}_{\mathrm{marker}} \times \overline{\mathbf{n}}_{d^{\mathrm{c}}}\,. \quad (28)$$

In order to solve for the static equilibrium configurations of the overall system, a director beam finite element formulation was used, which eventually led to the solution of an $f$-dimensional nonlinear equation $\mathbf{h}(\mathbf{z}) = 0$, where $\mathbf{z}$ are all the degrees of freedom of the discretized system, see [23] for further details. Since in Section III, the pressurization of the chambers appeared as contact forces and couples, only the rod's material law had to be adapted. In [24], it is also explained how the constraints (25) and (26) can be treated. All rods were discretized with one third order B-spline element. Increasing the element numbers did not further change the outcome.

In order to substantiate the modeling assumptions, three different models with increasing complexity were investigated.

*M0:* Linear material law [16] with constant radii $r_{\mathrm{p}_k} = r_{\mathrm{p}}$ and vanishing offset $\boldsymbol{\rho}^{\mathrm{off}} = \mathbf{0}$. The following parameters must be determined experimentally $c_{\mathrm{b}}, \boldsymbol{\beta} = (c_{\mathrm{e}})$.

*M1* ($\circ$): Ogden material law (16) with constant radii $r_{\mathrm{p}_k} = r_{\mathrm{p}}$ and vanishing offset $\boldsymbol{\rho}^{\mathrm{off}} = \mathbf{0}$. The following parameters must be determined experimentally $c_{\mathrm{b}}, \boldsymbol{\beta} = (c_{\mathrm{e}}, \alpha)$.

*M2* ($+$): Ogden material law (16) with constant radii $r_{\mathrm{p}_k} = r_{\mathrm{p}}$ and constant offset $\boldsymbol{\rho}^{\mathrm{off}} = \theta^{2,\mathrm{off}}\mathbf{d}_2 + \theta^{3,\mathrm{off}}\mathbf{d}_3$. The following parameters must be determined experimentally $c_{\mathrm{b}}, \boldsymbol{\beta} = (c_{\mathrm{e}}, \alpha, \theta^{2,\mathrm{off}}, \theta^{3,\mathrm{off}})$.

*M3* ($\times$): Ogden material law (16) with pressure-dependent radii $r_{\mathrm{p}_k}$ from (22) and constant offset $\boldsymbol{\rho}^{\mathrm{off}} = \theta^{2,\mathrm{off}}\mathbf{d}_2 + \theta^{3,\mathrm{off}}\mathbf{d}_3$. The following parameters must be determined experimentally $c_{\mathrm{b}}, \boldsymbol{\beta} = (c_{\mathrm{e}}, \alpha, \theta^{2,\mathrm{off}}, \theta^{3,\mathrm{off}}, c_{\mathrm{p}})$. The reference pressure was set to $p_{\mathrm{ref}} = 0.8\,bar$.

The parameters were identified in the following way and reported in Table IV. Initially, the parameters were set to $c_{\mathrm{b}} = 1, c_{\mathrm{e}} = 1, \alpha = 2, \theta^{2,\mathrm{off}} = \theta^{3,\mathrm{off}} = 0$ and $c_{\mathrm{p}} = 0$. Since both parameters $c_{\mathrm{b}}$ and $c_{\mathrm{p}}$ influence the overall bending stiffness of the actuator, first the parameter $c_{\mathrm{b}}$ was identified using the deflection data (24) of the bending experiment with unpressurized chambers such that the Euclidean error of the difference between the

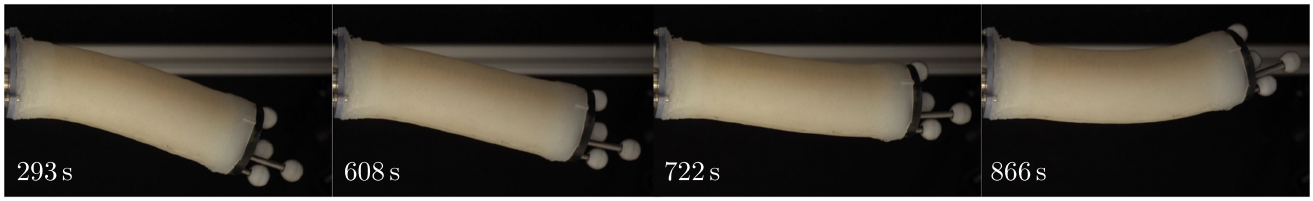


Fig. 8. Snapshots of the first half of the horizontal experiment. The left and right images show the initial and the maximally deformed configuration, respectively.

TABLE V
COST FUNCTIONS FOR TRAINING AND TEST SET

| | *M0* | *M1* | *M2* | *M3* |
|---|---|---|---|---|
| $K_{\text{training}}$ | 9.1 mm | 9.0 mm | 7.6 mm | 2.8 mm |
| $K_{\text{test}}$ | 11.4 mm | 11.3 mm | 11.4 mm | 4.9 mm |

measured and simulated coordinates of the actuator's end point

$$\boldsymbol{\delta} = (x - \overline{x}, y - \overline{y}, z - \overline{z}) \tag{29}$$

was minimized. This optimal value was then kept fixed for all subsequent pressurized experiments.

The remaining unknown parameters $\boldsymbol{\beta}$ of model *M0* to *M3* are identified during another optimization procedure using the training set, which consists of the $N = 4$ experiments $(i)$ and $(iii)$ for $M_i$ different static equilibria within each experiment. Using a Nelder-Mead simplex algorithm [25], the optimal values $\boldsymbol{\beta}^*$ were obtained for

$$\boldsymbol{\beta}^* = \underset{\boldsymbol{\beta}}{\operatorname{argmin}}\ K(\boldsymbol{\beta})\ ,\ \text{s.t.}\ \ \mathbf{h}(\mathbf{z}) = 0\ ,$$

$$K(\boldsymbol{\beta}) = \frac{1}{N}\sum_{i=1}^{N}\frac{1}{M_i}\sum_{j=1}^{M_i}\sqrt{\boldsymbol{\delta}_{ij}\cdot\boldsymbol{\delta}_{ij}}\ , \tag{30}$$

where $\boldsymbol{\delta}_{ij}$ denotes the difference (29) for the $j$th equilibrium point in the $i$th experiment. The cost function $K$ in (30) is the averaged deviation of the measured and simulated tip-displacement. In Table V, the cost functions are listed for the training set as well as for the test set, which consists of the experiments $(ii)$ and $a)$.

## VII. DISCUSSION

The necessity of the first model refinement that includes $\boldsymbol{\rho}^{\text{off}} \neq 0$ becomes immediately apparent when considering experiment $(iii)$, see Fig. 5 (bottom). Due to the symmetry of the second area of inertia in the constitutive laws (14) and (18), the axisymmetric loading due to gravity and equally pressurized chambers leads to an axisymmetric solution for model *M1*. The solution displayed in circles in Fig. 5 (bottom right) shows only an elongation in $\mathbf{e}_3$-direction, while the lateral displacements vanish. However, the experimental data show a behavior with deflections in both the $\mathbf{e}_2$- and $\mathbf{e}_3$-direction. As seen in the same plot, the constant offset $\boldsymbol{\rho}^{\text{off}}$ included in model *M2* and *M3* suffices to describe the observed asymmetric behavior. Consequently, in all the remaining plots, only the results of model *M2* and *M3* are displayed. As already mentioned earlier, when considering the pressurized part of the contact couples in (7), an offset from an ideal symmetric chamber distribution causes a model error that increases linearly in terms of the offset. In contrast, stiffness errors caused by the second area of inertia increase only quadratically, see Table III. This is the reason why for unpressurized rods fabrication errors do not drastically affect the rod's mechanical behavior.

In Fig. 6, the measurements and simulation data of experiment $(i)$ are plotted. For model *M2*, the parameters $\boldsymbol{\beta}$, which were optimized among others for this experiment, underestimate the deflections in lateral directions. The introduction of a pressure-dependent chamber radius (22) causes the desired increase in the actuation couple required for larger deflections, as seen in the results of model *M3*.

To show the model's predictability, we used experiments $(ii)$ and $a)$ as test sets. In Fig. 7, both model *M2* and *M3* underestimate the deflection. Again, the actuation in model *M2* is much weaker than in model *M3*, which definitively justifies the change of pressure radii. An interpretation of the underestimation of model *M3* is that the two simultaneously actuated pressure chambers interact in such a way that a further increase of the actuation couple is obtained. The advantage of a physically motivated model becomes apparent when changing completely the configuration. Then also in the horizontally mounted configuration, see Figs. 5 (top) and 8, a very good predictive behavior was achieved for model *M3*.

Comparing the averaged tip-displacement deviations in Table V, the major model improvement is obtained by the pressure-dependent chamber radii (22).

## VIII. CONCLUSION

To describe the deformation of a soft pneumatic actuator with three pressure chambers, we developed a pressure-dependent spatial nonlinear rod theory. The equilibrium equations of the rod (10) followed from a three-dimensional continuum theory by restricting the placement function of the body. During this reduction procedure, the pressurization of the chambers revealed as part of the resultant contact forces and couples. Consequently, the pressurization of the chambers can be considered as part of the rod's constitutive laws, which relate the contact forces and couples with the rod's kinematics and the pressures. There are several benefits from this point of view. For an established spatial beam finite element implementation, as for instance [26], [27], including a new pressure-dependent material is sufficient to account for the pressurization effect. Additionally, also contributions of pressure chambers with variable cross-sections and changing distance to the rod's centerline can be included straightforwardly. To describe the experimentally observed

behavior of the actuator, two additional refinements were considered. With a constant displacement $\boldsymbol{\rho}^{\text{off}}$ of all pressure chambers within the cross-sections, the asymmetric behavior for a pressure actuation $p_1 = p_2 = p_3 = p$ could be explained. The increasing strength of the actuator with increasing pressure was captured heuristically by a linear change of the pressure chamber radius. In order to explain this behavior in more detail, one needs to introduce a rod theory that also accounts for cross-section deformation, see for instance [28]. For the material part of the actuator's constitutive laws, we suggested a nonlinear material behavior considering the strengthening behavior of silicone under tension.

With the solution of the governing equations of the rod by beam finite elements, we presented an established (in the field of structural mechanics) alternative to the shooting method which is very popular in robotics, [16]. The actuator was composed of three interconnected rods. This showed how straightforwardly an assembly of various rods can be treated with beam finite elements. The same holds also if several actuators act in parallel. An extension of the model to dynamics follows directly by adding the rods inertial virtual work contributions as for instance formulated in [13], [14]. Depending on the rotation parametrization, the finite element discretization then leads either to a set of ordinary differential equations or differential algebraic equations that must be solved, see [23]. However, in a dynamic simulation it is expected that the modeling of the pressure build-up is also crucial. Since the number of elements was rather low, real-time capability is at reach and must be investigated. The model will definitively assist a future design of a more complex manipulator made of several stacked actuators.

## REFERENCES


[1] K. Suzumori, S. Iikura, and H. Tanaka, "Flexible microactuator for miniature robots," in *Proc. IEEE Micro Electro Mech. Syst.*, 1991, pp. 204–209.

[2] A. D. Marchese, R. Tedrake, and D. Rus, "Dynamics and trajectory optimization for a soft spatial fluidic elastomer manipulator," *Int. J. Robot. Res.*, vol. 35, no. 8, pp. 1000–1019, 2016.

[3] I. S. Godage, R. Wirz, I. D. Walker, and R. J. Webster, "Accurate and efficient dynamics for variable-length continuum arms: A center of gravity approach," *Soft Robot.*, vol. 2, no. 3, pp. 96–106, 2015.

[4] S. H. Sadati, S. E. Naghibi, I. D. Walker, K. Althoefer, and T. Nanayakkara, "Control space reduction and real-time accurate modeling of continuum manipulators using Ritz and Ritz-Galerkin methods," *IEEE Robot. Automat. Lett.*, vol. 3, no. 1, pp. 328–335, Jan. 2017.

[5] J. Fras, M. Macias, Y. Noh, and K. Althoefer, "Fluidical bending actuator designed for soft octopus robot tentacle," in *Proc. IEEE Int. Conf. Soft Robot.*, 2018, pp. 253–257.

[6] S. Kolachalama and S. Lakshmanan, "Continuum robots for manipulation applications: A survey," *J. Robot.*, vol. 2020, pp. 4187048:1–19, 2020.

[7] R. Kang, D. T. Branson, E. Guglielmino, and D. G. Caldwell, "Dynamic modeling and control of an octopus inspired multiple continuum arm robot," *Comput. Math. Appl.*, vol. 64, no. 5, pp. 1004–1016, 2012.

[8] H. Habibi, C. Yang, I. Godage, R. Kang, I. Walker, and D. Branson, "A lumped-mass model for large deformation continuum surfaces actuated by continuum robotic arms," *J. Mechanisms Robot.*, vol. 12, pp. 1–12, 2020.

[9] K. Suzumori, T. Maeda, H. Wantabe, and T. Hisada, "Fiberless flexible microactuator designed by finite-element method," *IEEE/ASME Trans. Mechatronics*, vol. 2, no. 4, pp. 281–286, Dec. 1997.

[10] C. Duriez, "Control of elastic soft robots based on real-time finite element method," in *Proc. IEEE Int. Conf. Robot. Automat.*, 2013, pp. 3982–3987.

[11] S. Neppalli, M. A. Csencsits, B. A. Jones, and I. D. Walker, "Closed-form inverse kinematics for continuum manipulators," *Adv. Robot.*, vol. 23, no. 15, pp. 2077–2091, 2009.

[12] R. J. Webster III and B. A. Jones, "Design and kinematic modeling of constant curvature continuum robots: A review," *Int. J. Robot. Res.*, vol. 29, no. 13, pp. 1661–1683, 2010.

[13] S. S. Antman, *Nonlinear Problems of Elasticity*, 2nd ed. New York, NY, USA: Springer, 2005.

[14] S. R. Eugster, *Geometric Continuum Mechanics and Induced Beam Theories*. Berlin, Germany: Springer, 2015.

[15] F. Renda, C. Armanini, V. Lebastard, F. Candelier, and F. Boyer, "A geometric variable-strain approach for static modeling of soft manipulators with tendon and fluidic actuation," *IEEE Robot. Automat. Lett.*, vol. 5, no. 3, pp. 4006–4013, Jul. 2020.

[16] J. Till, V. Aloi, and C. Rucker, "Real-time dynamics of soft and continuum robots based on Cosserat rod models," *Int. J. Robot. Res.*, vol. 38, no. 6, pp. 723–746, 2019.

[17] J. Till, V. Aloi, K. E. Riojas, P. L. Anderson, R. J. Webster III, and C. Rucker, "A dynamic model for concentric tube robots," *IEEE Trans. Robot.*, vol. 36, no. 6, pp. 1704–1718, Dec. 2020.

[18] M. Bartholdt, M. Wiese, M. Schappler, S. Svenja, and A. Raatz, "A parameter identification method for static cosserat rod models: Application to soft material actuators with exteroceptive sensors," in *Proc. IEEE/RSJ Int. Conf. Intell. Robots Syst.*, 2021, pp. 624–631.

[19] S. R. Eugster, C. Hesch, P. Betsch, and Ch. Glocker, "Director-based beam finite elements relying on the geometrically exact beam theory formulated in skew coordinates," *Int. J. Numer. Methods Eng.*, vol. 97, no. 2, pp. 111–129, 2014.

[20] S. R. Eugster and J. Harsch, "A variational formulation of classical nonlinear beam theories," in *Developments and Novel Approaches in Nonlinear Solid Body Mechanics*. Berlin, Germany: Springer, 2020, pp. 95–121.

[21] L. Marechal, P. Balland, L. Lindenroth, F. Petrou, C. Kontovounisios, and F. Bello, "Toward a common framework and database of materials for soft robotics," *Soft Robot.*, vol. 8, no. 3, pp. 284–297, 2021.

[22] R. W. Ogden, *Non-Linear Elastic Deformations*. New York, NY, USA: Dover, 1997.

[23] J. Harsch, G. Capobianco, and S. R. Eugster, "Finite element formulations for constrained spatial nonlinear beam theories," *Math. Mechanics Solids*, vol. 26, no. 12, pp. 1838–1863, 2021.

[24] J. Harsch and S. R. Eugster, "Finite element analysis of planar nonlinear classical beam theories," in *Developments and Novel Approaches in Nonlinear Solid Body Mechanics*. Berlin, Germany: Springer, 2020, pp. 123–157.

[25] F. Gao and L. Han, "Implementing the Nelder-Mead simplex algorithm with adaptive parameters," *Comput. Optim. Appl.*, vol. 51, no. 1, pp. 259–277, Jan. 2012.

[26] A. Cardona and M. Geradin, "A beam finite element non-linear theory with finite rotations," *Int. J. Numer. Methods Eng.*, vol. 26, no. 11, pp. 2403–2438, 1988.

[27] I. Romero, "The interpolation of rotations and its application to finite element models of geometrically exact rods," *Comput. Mechanics*, vol. 34, no. 2, pp. 121–133, 2004.

[28] I. Giorgio, "A discrete formulation of Kirchhoff rods in large-motion dynamics," *Math. Mechanics Solids*, vol. 25, no. 5, pp. 1081–1100, 2020.